Proceedings of ASME Turbo Expo 2011
GT2011
June 6-10, 2011, Vancouver, British Columbia, Canada

GT2011-46686

PROBABILISTIC HIGH-CYCLE FRETTING FATIGUE ASSESSMENT OF GAS TURBINE ENGINE COMPONENTS

Kwai S. Chan **Michael P. Enright**

Southwest Research Institute®
San Antonio, TX 78238, USA

Patrick J. Golden

Air Force Research Laboratory
Wright-Patterson AFB, OH 45433, USA

Samir Naboulsi

High Performance Technologies, Inc.,
Wright-Patterson AFB, OH 45433, USA

Ramesh Chandra **Alan C. Pentz**

NAVAIR
Patuxent River, MD 20670, USA

ABSTRACT

High-cycle fatigue (HCF) is arguably one of the costliest sources of in-service damage in military aircraft engines. HCF of turbine blades and disks can pose a significant engine risk because fatigue failure can result from resonant vibratory stresses sustained over a relatively short time. A common approach to mitigate HCF risk is to avoid dangerous resonant vibration modes (first bending and torsion modes, etc.) and instabilities (flutter and rotating stall) in the operating range. However, it might be impossible to avoid all the resonance for all flight conditions. In this paper, a methodology is presented to assess the influences of HCF loading on the fracture risk of gas turbine engine components subjected to fretting fatigue. The methodology is based on an integration of a global finite element analysis of the disk-blade assembly, numerical solution of the singular integral equations using the CAPRI (Contact Analysis for Profiles of Random Indenters) and Worst Case Fret methods, and risk assessment using the DARWIN (Design Assessment of Reliability with Inspection) probabilistic fracture mechanics code. The methodology is illustrated for an actual military engine disk under real life loading conditions.

1 INTRODUCTION

Premature cracking has been observed in several engine disks in military aircraft. Available data suggest that fretting fatigue may be a strong contributor to the premature formation of fatigue cracks in these engine disks. To better assess the risk of disk failure, a probabilistic fatigue crack growth (FCG) methodology has been previously developed for treating fretting fatigue by considering the stress variability [1], inspection intervals [2], material variability [2], and risk mitigation by locally-induced residual stresses [3, 4]. The methodology is based on an integration of a global finite element analysis of the disk-blade assembly [5] and associated contact stresses [6 ,7], small-crack fretting fatigue modeling [7], and risk assessment using the DARWIN (Design Assessment of Reliability with Inspection) probabilistic fracture mechanics code [8]. The methodology has been demonstrated for an actual military engine disk under real life loading conditions. The influence of inspection and residual stress on potential risk reduction has been investigated for simulated mission profiles typical of those associated with low-cycle fatigue (LCF). The contribution of high-cycle vibratory stresses to the risk of engine failure has not been considered in the previous studies [1-4].

High-cycle fatigue (HCF) has been identified as one of the costliest in-service damages in military aircraft engines [9, 10]. HCF of turbine blades and disks can pose a significant engine risk because fatigue failure can result from resonant vibratory stresses sustained over a relatively short time. One approach to mitigate HCF risk is to avoid dangerous resonant vibration modes (first bending and torsion modes, etc.) and instabilities (flutter and rotating stall) in the operating range [11-14]. However, it might be difficult to avoid resonance for all flight conditions and stall flutter can be induced unknowingly. Thus, substantial efforts have been spent in recent years to develop computational methods for analysis and prediction of the resonance forced response of bladed disks. Gallagher *et al*. [15] published a detailed report addressing key issues associated with developing, verifying, and implementing a material damage tolerant design methodology capable of predicting HCF limits and material thresholds for Ti-6Al-4V. The methodology development was extended to another titanium alloy, Ti-17, and to a nickel-base single crystal alloy, PWA 1484. This program was a follow-on effort to a program on Improved High Cycle Fatigue (HCF) Life Prediction, USAF Contract F33615-96-C-5269.

Hilbert *et al*. [16] developed a stress prediction method for airfoil response due to gas path excitation. The method predicted the response characteristics measured in a full engine test. The complexity of the airfoil mode shape and unsteady pressure distribution required a three-dimensional analysis. Marshall and Green [17] applied a three-dimensional (3D) linearized Euler method for obtaining response. The transient dynamic results were broadly in very good agreement with the experimental data. The speed of the resonances was predicted to be in the range 79-81% speed for the 36 engine order (EO), corresponding to a frequency of 5090 Hz. The experimental value was 77%, corresponding to a frequency of around 4950 Hz. Sayma *et al*. [18] presented a force response analysis of a military engine lift fan. The analysis was performed using an integrated aeroelasticity model which combines a non-linear, time-accurate, viscous unsteady flow representation with a modal model of the structure. A 15 million point grid was used in all forced response calculations which were run in parallel mode on an MPI cluster. A single calculation required 8 GB RAM and took two weeks on four 600 MHz EV6 Alpha processors. The computed blade responses were compared to measured data and the worst case was under-predicted by 50%. The predictions were considered to be satisfactory because of complexities in the computations and boundary conditions. Panovsky *et al*. [19] predicted the response of high pressure turbine blade using CFD code TURBO and compared to experimental results. TURBO is a 3D, unsteady, multiple blade row Navier-Stokes code developed at Mississippi State University. The test data was generated in the Gas Turbine Laboratory at Ohio State University. The results included unsteady pressure on the blade surface as well as vibratory response levels at two axial spacings for several modes. Predictions of aero damping for these modes are also compared to measurements made during the forced response tests. Petrov [20] investigated the influence of the contact interfaces parameters on nonlinear vibrations of bladed discs via direct method. In particular, forced response levels were calculated directly as a function of contact interface parameters such as the friction coefficient, normal and tangential stiffness coefficients, clearances, interferences, and the normal stresses at the contact interfaces. Special contact interface elements were developed providing exact sensitivity coefficients with respect to variation of all parameters of the friction contact interfaces. Application of this method to practical bladed discs demonstrated its high efficiency. In summary, computing the blade's aerodynamic loading in a jet engine is a complex process and generally requires a combined experimental and computational analysis [16-23].

The objective of the present study was to probabilistically investigate the high-cycle fatigue assessment of blade/disk assembly in a gas turbine engine. To simplify the analysis and focus on the fatigue assessment, a reasonably accurate aerodynamic loading model was provided by NAVAIR and utilized to perform the computational structural-mechanical analysis of a blade/disk assembly. In particular, structural analyses of a blade/disk assembly were performed via the FEM method to compute the static and dynamic contact stresses, and the bulk stresses associated with stall flutter conditions. The computed dynamic stresses were calibrated using blade tip displacements from existing engine test data. In addition, the computed dynamic stresses at the blade root were verified using strain gauge measurements from engine test data. Subsequently, stall-flutter-induced vibratory stresses were incorporated into a simplified composite mission, which was then utilized to compute the contact stress distribution at the blade/disk attachment using the singular-integral-equation techniques. The LCF and HCF load histories were then used in conjunction with pertinent probabilistic life-prediction methods for assessing fatigue crack growth due to the combined LCF and HCF stresses in engine disks and the risk of disk fracture with and without the presence of high-cycle vibratory stresses.

2 LOAD HISTORIES FOR HIGH-CYCLE VIBRATORY STRESS

The current methodology developed by the authors [1-4] for treating low-cycle fretting fatigue crack growth relies on the use of a simplified mission to compute the global contact forces at the blade/disk interface using a 3D finite-element analysis approach. Fig. 1 illustrates a typical fan speed profile based on the composite mission associated with actual engine usage histories [1]. The simplified mission, shown in Fig. 1, is comprised of about 24 major and minor speed reversals which have been utilized to establish the load histories required for low-cycle fretting fatigue crack growth analyses in previous work. The simplified mission profile, however, does not provide sufficient information for establishing the high-cycle vibratory load histories. The potential sources of vibratory stresses on gas turbine blades are resonance, flutter, and rotating stall. Regions of stall flutter can be mapped and displayed in a map of pressure ratio versus corrected airflow. Literature data indicate that two stall flutter regions may exist: one at about 60-70% of the max speed and one at higher engine speeds. In this investigation, high-cycle vibratory stresses related to stall flutter near 72% max engine speed, shown by the red line in Fig. 1, were considered.

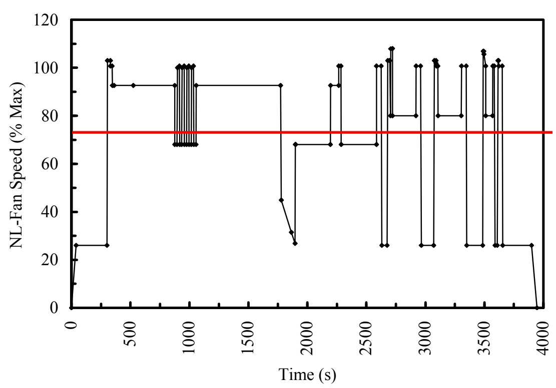

Fig. 1. Typical fan speed profile based on the composite mission. Points indicate load steps. From Chandra *et al.* [1].

Existing engine test data generated to map out the stall flutter regions of a military engine were utilized to establish the high-cycle vibratory load histories. The stall flutter frequency was identified from a Campbell diagram, Fig. 2, by following frequency signals that ride along an engine order line and then deviate from the engine order line. The non-integral excitation frequency between engine order lines was taken as the stall flutter frequency, f_{SF}, and the corresponding engine speed was noted.

The duration of stall flutter was identified by tracking the peak-to-peak strain signals, Fig. 3, at the stall flutter frequency from strain gauges placed on the airfoil and the root of several instrumented blades. The time span measured at the half-height of individual strain peaks during a flutter event was taken as the duration of stall flutter. Typically, the duration of a stall flutter event ranged from less than 1 second to a few seconds. The peak-to-peak strain data also provided the vibratory stresses at various locations at the airfoil, blade root, and the disk during stall flutter. The vibratory stresses at various locations at the airfoil and the blade root were normalized by those at the disk and the normalized dynamic stresses are presented in Fig. 4. Figure 4 indicates that the dynamic stresses at locations 2 and 3 in the airfoil are about ten times that at location Y in the disk. At the blade root, the dynamic stress ranged from 1 to 5 times that at location Y in the disk.

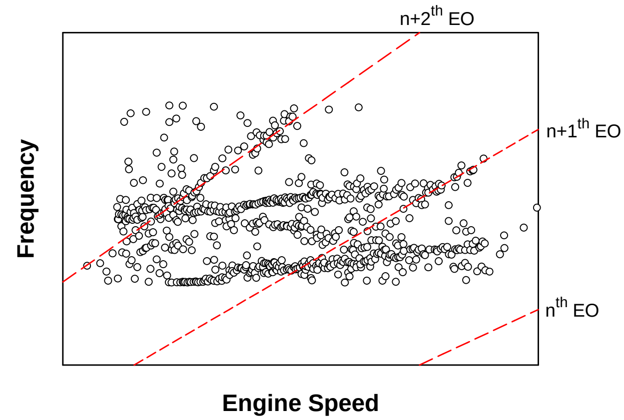

Fig. 2. Campbell diagram showing excitation at a frequency that deviates from integral engine order lines at about 72% max. engine speed.

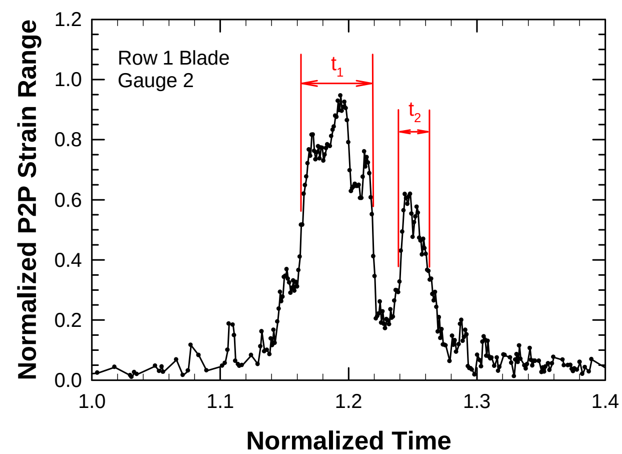

Fig. 3. Peak-to-peak (P2P) strain data as a function of time during stall flutter.

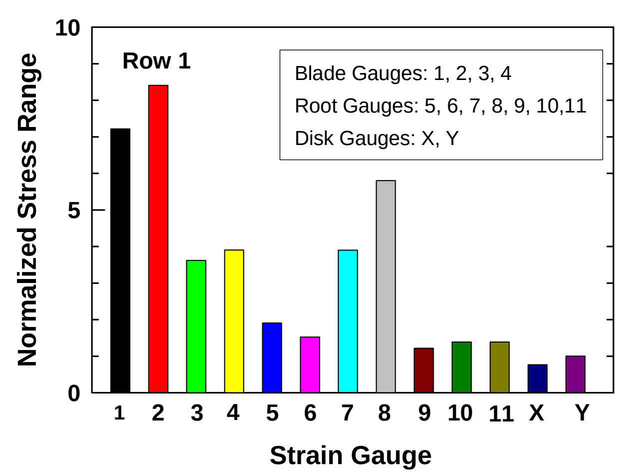

Fig. 4. Dynamic stresses at various locations at the airfoil and the blade root normalized by the dynamic stress at location Y in the disk.

3 COMBINED LOAD HISTORIES FOR LOW-CYCLE AND HIGH-CYCLE FRETTING FATIGUE STRESS

A finite element method analysis of the disk-blade assembly was carried out to obtain contact forces and moments along the disk-blade interface. Due to the complex geometry of the fan blade, higher order tetrahedral elements (C3D10) were used for the associated finite element mesh. A refined mesh of first order hexahedral elements (C3D8) was used for the dovetail portion of the fan blade and the disk [24]. This element type was selected for its superior performance in the contact interface.

The FEM mesh for the disk-blade assembly and for the interface region between the dovetail portion of the blade and the disk is shown in Figs. 5 and 6, respectively. The dovetail is aligned along the axial direction of the engine. A single blade and section of the disk were modeled using cyclic symmetry to represent the entire rotor. The entire mesh had approximately 121,000 elements including 800 elements in contact on the disk side of the interface and approximately 400 elements on the dovetail side of the interface. The model was solved using the ABAQUS 6.9 software [25] using a surface-to-surface contact formulation.

The simplified mission shown in Fig. 1 was utilized as the starting point for building the loading histories for the combined low-cycle and high-cycle fretting fatigue analysis. The mission profile in Fig. 1 includes 22 speed reversals and includes both major and minor reversals. Load cases available for low-cycle fatigue analysis included 50%, 72%, and 110% maximum fan speed. A simple mission (0%, 110%, 50%, 110%, and 72%) was built for the FEM analysis that would allow contact force history effects to be analyzed. The simplified mission was used in order to limit the computational time needed for the analysis and to coincide with the fan speeds where the aerodynamic loads were available. Convergence of the nonlinear analysis required that each load step in the mission be broken into 15-25 increments, resulting in a total of 87 increments available for post-processing. For analyzing high-cycle fretting fatigue, dynamic stress analyses of the blade/disk assembly were performed by exciting the assembly at the frequency and engine speed of interest; both were determined from the engine data for stall flutter condition at about 72% of the maximum engine speed.

For the dynamic analysis, an implicit time dependent direct integration method was selected because of the need for the computation of the nonlinear contact fretting fatigue stresses. The disadvantage of using the implicit time method was that it was computationally expensive. In this study, a DoD High Performance Computing resource was used to speed up the computation.

The dynamic stresses due to LCF and HCF loading conditions were calculated as follows. First, a static nonlinear stress analysis was performed to simulate a 72% inertia loading (*i.e.,* including the nonlinear contact stresses at the blade/disk dovetail interface surface). Second, a reasonably accurate aerodynamic pressure loading model provided by NAVAIR was used to simulate the aerodynamic loading, and equivalent nodal aerodynamic forces were applied on the blade surface. These forces were applied harmonically at the critical frequency and LCF loading level determined from engine test data. Third, the computational model was calibrated based on available engine test data until the computed and measured blade tip displacements were in agreement. The calibration was performed by applying a constant factor to the aerodynamic nodal forces. This factor value was determined by trying various values and selecting the one that corresponded to the desired blade tip displacement. Once the computed blade tip displacement matched the experimentally observed value from engine test data, the corresponding aerodynamic loads were selected and utilized to compute dynamic stresses for the blade/disk assembly. Dynamic stresses at various locations of the blade were then compared

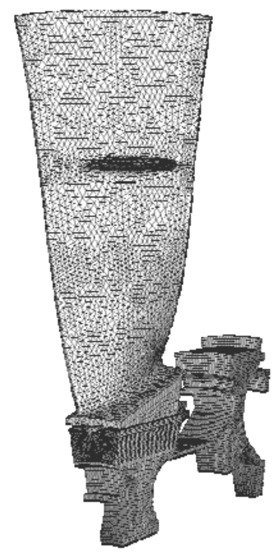

Fig. 5. Finite element mesh of blade/disk assembly.

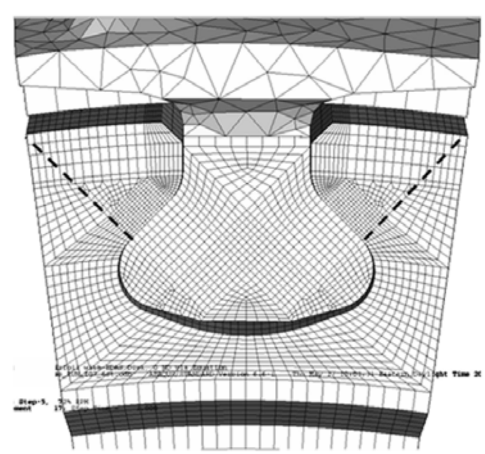

Fig. 6. A refined mesh of first order hexahedral elements (C3D8) for the dovetail portion of the fan blade and the disk.

against peak-to-peak (P2P) stresses from strain gauge data located at thirteen locations of the blade/disk assembly (four on the air foil, seven on the blade root, and two on the disk). Figure 7 shows a comparison of the computed and measured values of the dynamic stresses (stress ranges) at several locations of the blade root during stall flutter at 72% maximum RPM. This is an independent comparison since none of the strain gauge data were used to calibrate the computational model – the computational model was calibrated using the tip displacement only. In general, the dynamic stresses at the root section were comparatively low. The region with the highest dynamic stresses was predicted to be location 7, in agreement with the engine data. In addition, the computed dynamics stress at location 7 was within 14% of the measured value. Overall, the agreement between the computed and the measured dynamic stress ranges (highest peak-to-peak values) were about 14% to 54%.

After validation against engine test data, the dynamic stresses were combined with the LCF stresses in the fatigue crack growth analyses for different combinations of LCF and HCF loads. Figure 8 shows the profiles of the stress versus cycle for both LCF and HCF loads. In particular, the HCF cycles were computed from the stall flutter frequency, the duration of a stall flutter event as determined from the width of the peak-to-peak of the dynamics strains measured during stall flutter, and the number of times the engine speed passes through the stall flutter condition, which is represented by the line at 72% maximum engine speed in Fig. 1. The HCF stresses occur after each speed reversal in the simplified mission profile. For computational efficiency, all HCF cycles have been appended at the end of the simplified mission profile to follow the LCF cycles. Figure 8 shows schematically the combined LCF and HCF stress histories, which consist of an LCF block with 24 cycles, followed by an HCF block with 8,702 cycles. Only 80 HCF cycles are shown in Fig. 5. HCF blocks with 33,630 cycles and 58,800 cycles have also been investigated.

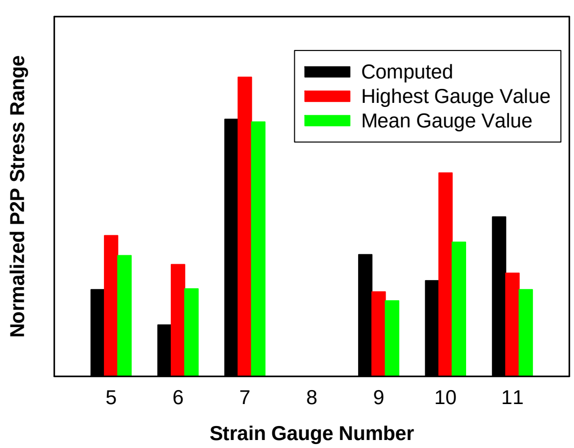

Fig. 7. A comparison of computed and measured peak-to-peak stress ranges normalized by a constant for various strain gauges in the root section.

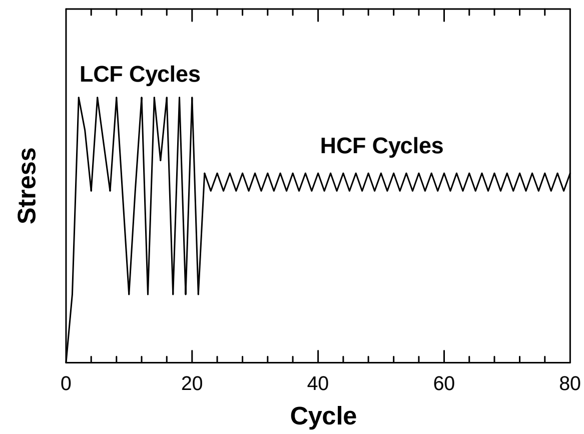

Fig. 8. Combined LCF and HCF load history for a composite mission profile.

4 CONTACT STRESS FOR LOW-CYCLE AND HIGH-CYCLE FRETTING FATIGUE ANALYSIS

The finite-element results were used to predict the contact normal force, P, shear force, Q, and contact moment, M, all per unit thickness, via the method developed by Gean and Farris [26]. In general, the blade force is proportional to the square of the rotor speed, Ω [26]:

$$F_{blade} = \sum\left[h_i \cdot \left(P_i \cos\theta + Q_i \sin\theta\right)\right] \propto \Omega^2 \tag{1}$$

where P_i and Q_i are the P and Q values for individual zones that are subdivided to model the attachment region of a disk. The sum of the radial components of P and Q times their slice thickness h must equal the total radial force applied by the blade, as shown in Eq. (1).

Once the high-cycle vibratory forces on a blade were known, they were incorporated into an FEM structural analysis to compute the global contact loads, P and Q, due to the LCF and HCF loading. Figure 9 shows schematically a representation of the dovetail geometry of the attachment region of a disk with a vibrating blade. The main LCF load is the radial load, $R(t)$, applied to the blade. Excitation is assumed to induce a high-cycle vibratory force, $\Delta G_{HCF}(t)$, in the tangential direction. A vibratory force, $\Delta R_{HCF}(t)$, in the radial direction is assumed here, but it may be negligibly small.

Applying the Gean and Farris analysis [26] leads to the P and Q expressions given by

$$P_{\max} = P_m + \frac{1}{2}\Delta P_{HCF} \tag{2}$$

$$Q_{\max} = Q_m + \frac{1}{2}\Delta Q_{HCF} \tag{3}$$

where the mean values of P and Q (P_m and Q_m) are functions of $R(t)$, the LCF load on the blade. The vibratory values of P and Q (ΔP_{HCF} and ΔQ_{HCF}) are contributed by the vibratory loads acting on the blade and are functions of both $\Delta R_{HCF}(t)$

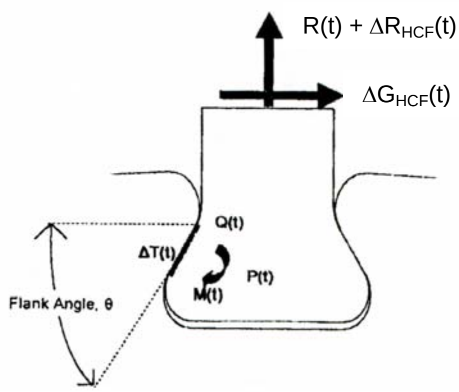

Fig. 9. Dovetail geometry subjected to radial load *R(T)* and $\Delta R_{HCF}(T)$ and $\Delta G_{HCF}(T)$ due to high-cycle flow-induced vibration. Modified from Gean and Farris [18].

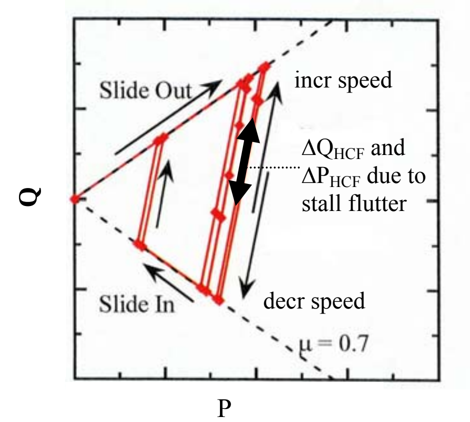

Fig. 10. Q and P history for a typical fan speed profile with $\Delta P_{HCF}(t)$ and $\Delta Q_{HCF}(t)$ due to high-frequency forced vibrations due to stall flutter.

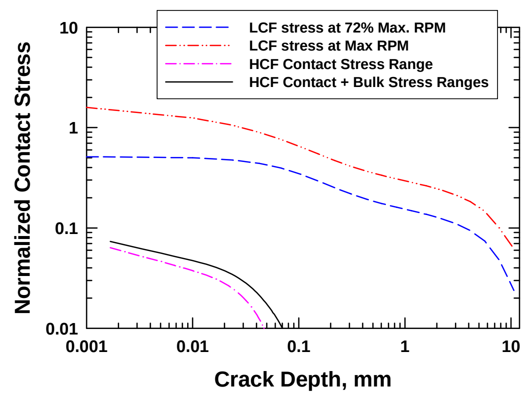

Fig. 11. A comparison of the LCF stresses at maximum RPM, 72% maximum RPM, HCF maximum and minimum stresses at 72% maximum RPM, and HCF stress range at 72% maximum RPM as a function of crack depth.

and $\Delta G_{HCF}(t)$. In addition, the minimum values of *P* and *Q* (P_{min} and Q_{min}) are given by Eqs. (2) and (3), but the + sign is replaced with the – sign. Since the blade passing frequency is expected to occur at a percentage of the maximum engine speed, the HCF vibratory forces are expected to oscillate at the (P_m, Q_m) point in a *P-Q* plot, as shown in Fig. 10, during an engine run-up or rundown event. Flutter-induced vibrations may occur at different engine speeds and thus may reside along different lines in the *P-Q* diagram. Once the *P*s and *Q*s are computed from the Gean and Farris type analysis [26], the contact stresses at the attachment region can be computed via one of two analytical codes based on the singular-integral-equations approach, the CAPRI code [6] or the Worst Case Fret (WCF) model [7]. The CARPI and the WCF codes, which were benchmarked previously, gave identical contact stresses for the input values of P and Q [2]. In this study, the contact stresses for the LCF loads were computed using CAPRI. Subsequently, the contact stresses associated with the HCF loads were computed using the WCF code [7] on the basis of the P, Q, ΔP, and ΔQ. The HCF bulk stresses were computed on the basis of the dynamic stresses measured at two locations on the disk and the bulk stress distribution function derived from the computed LCF stresses at 72% maximum RPM.

Figure 11 presents the LCF contact stresses for the 72% and the maximum engine speed as a function of distance from the contact surface. Also presented in Fig. 11 are the LCF contact stresses at 72% maximum speed and the HCF stresses. The HCF contact stress ranges with and without the HCF bulk stresses are presented in Fig. 11; both are considerably lower that the LCF stresses. It is also important to note that the HCF contact stresses extend to a shallow depth (about 200 μm) below the contact surfaces.

5 CRACK GROWTH MODELING AND LIFE PREDICTION

Once the contact stress and bulk stress are computed, the FCG life can be predicted for the combined LCF and HCF load histories. For the deterministic fracture mechanics assessment, the disk blade attachment region can be modeled as a rectangular plate with a semicircular surface crack placed along the edge of contact. The stress intensity factors can be computed using a weight-function-based surface crack stress intensity factor solution that includes a correction for small crack effects via the small-crack parameter, a_o [27]. The crack path can be taken to be at a 20° angle from the normal to the attachment surface where the interior stress ranges are highest [2]. This particular crack angle also corresponds to the observed crack growth direction in fretting fatigue experiments and in failed disks reported in the literature [2]. Crack growth rate values have been obtained using a crack growth model [28] fit to the material data.

The crack growth rate equation describes all three regions of the large-crack FCG curve and is given by [28]

$$\frac{da}{dN} = C\left(\frac{(1-f)\Delta K}{1-R}\right)^n \frac{\left(1-\frac{\Delta K_{th}}{\Delta K}\right)^p}{\left(1-\frac{K_c}{K_{\max}}\right)^q} \tag{5}$$

where C and n are empirical constants for the power-law region. The parameter p is an empirical constant describing the large-crack threshold region, ΔK_{th}, and the parameter q describes the fast fracture region where the maximum K, K_{max}, approaches the critical stress intensity at fracture, K_C. The parameter f is the ratio of K_{op}/K_{max}, where K_{op} is the stress intensity factor at which the crack tip is fully open. The presence of a compressive residual increases K_{op} and thus reduces the effective ΔK, which is the difference between K_{max} and K_{op}. The value of f is computed in DARWIN using the Newman crack closure model [29].

The fatigue crack growth analyses were performed by treating the LCF and HCF loads as the random variables, while keeping the HCF time duration during stall flutter as a deterministic parameter. The median and COV of the LCF stress random variable were calibrated to available crack growth life data (the details of the calibration are described in Enright et al. [4]). The median of the HCF stress random variable was calibrated based on blade tip displacements as previously described. The COV of the HCF stress random variable was based on the scatter in HCF stress values associated with strain gage measurements obtained at various locations within the disk. Three different time durations (t_1, t_2, and t_3) were investigated. These time durations encompassed the excitation times during ascent, stall flutter, and descent. Figure 12 shows a comparison of the computed crack areas as a function of flight hours for LCF loads with and without HCF vibratory loads. Results for HCF blocks with three different flutter durations (t_1, t_2 and t_3) are presented in Fig. 12. The value of t_2 is on the order of the mean. The comparison shows that the presence of the HCF vibratory stresses reduced the flight hours to fracture by 39%, 60%, and 65% for t_1, t_2 and t_3, respectively. For these particular computations, one of the mission profiles contained 24 LCF load cycles and 8,702 HCF cycles; the latter corresponded a stall flutter duration (t_1) of the shortest time observed per event. Increasing the stall flutter duration to t_2 or t_3 reduced the flight hours at fracture by 60% to 65%, compared to the LCF life without HCF loads.

Fracture risk computations were performed using DARWIN [30]. Normalized probability of fracture results are shown in Fig. 13 for LCF loading without and with HCF loads, respectively. For HCF loading, results for the time durations of t_1, t_2, and t_3 are presented. From these results, it can be concluded that the risk of disk fracture is increased by the presence of HCF loads with the shortest flutter time direction (t_1). Increasing the time duration from t_1 to t_2 further reduces the fatigue rack growth life and increases the risk of fracture, but both occur at diminishing rates. A further increase in the flutter time duration to t_3 causes only a small decrease in life and a small increase in risk. Since the HCF contact stresses concentrate mostly in a region that extends up to about 200 μm below the surface, a further increase in the flutter time duration that is larger than t_3 may not cause a further decrease in life or increase in risk once the crack depth exceeds 200 μm and the HCF stresses drop to very low values (Fig. 11).

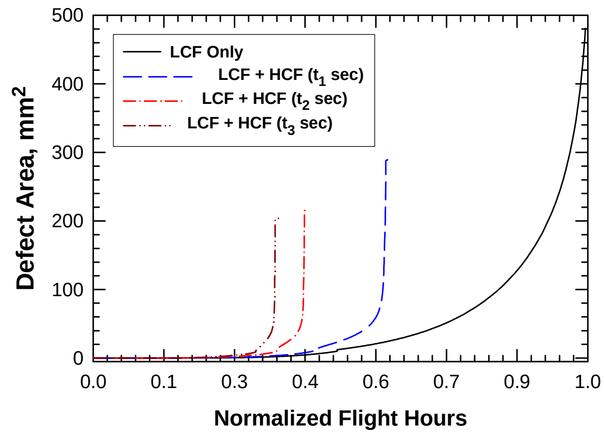

Fig. 12. A comparison of the predicted flight hours with and without the presence of HCF loads.

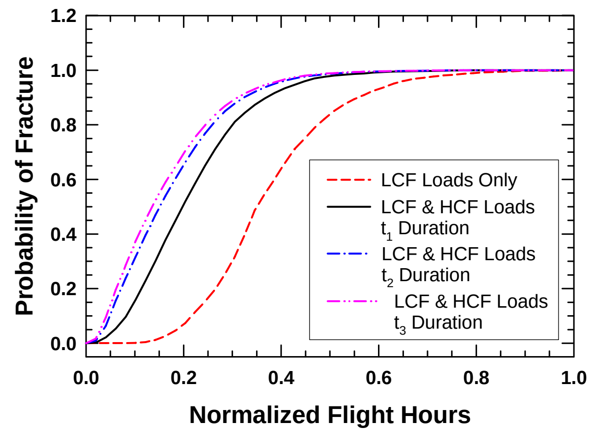

Fig. 13. Comparisons of fracture risk of engine disk without and with HCF loads due to stall flutter.

6 DISCUSSION

The results presented in this paper are works in progress that are intended to illustrate the HCF life-prediction methodology. First, the computations relied on the dynamic stress ranges at the blade root derived from matching the tip displacement from existing engine test data. The corresponding computed dynamic stresses at the blade root are in reasonable agreement with the strain gauge measurements at the blade root. This suggests that the blade tip displacement is a reasonably accurate and viable method for calibrating FEM dynamic stress computation to real-life engine test data for establishing and verifying dynamic stress calculations.

The number of HCF fatigue cycles required for the HCF portion of the mission profile is quite large. A range of time durations was observed during stall flutter. Computational results for three time durations are presented in Fig. 12. In the current computations, all HCF stress pairs were used in the crack growth analysis and no fatigue threshold check was performed. In future work, fatigue crack growth threshold checks will be considered. The threshold check may reduce the number of HCF stress ranges and the computation times required in the fatigue crack growth rate computation.

The computational results indicate that the HCF stress ranges at the blade root and the blade/disk interface are small and the fatigue crack growth rates are typically low. The HCF stresses are sufficiently low and they are present only when the crack length is small (10-200 μm), as shown in Fig. 14. Despite limited magnitudes, the HCF stresses contribute to the fatigue crack growth process because the number of HCF cycles was sufficiently large that the small HCF loads led to some reduction in flight hours once the fatigue threshold can be exceeded by the HCF stresses alone. For the cases considered, HCF crack growth occurs when the HCF stresses are near or above the 95% confidence limits, as shown in Fig. 14.

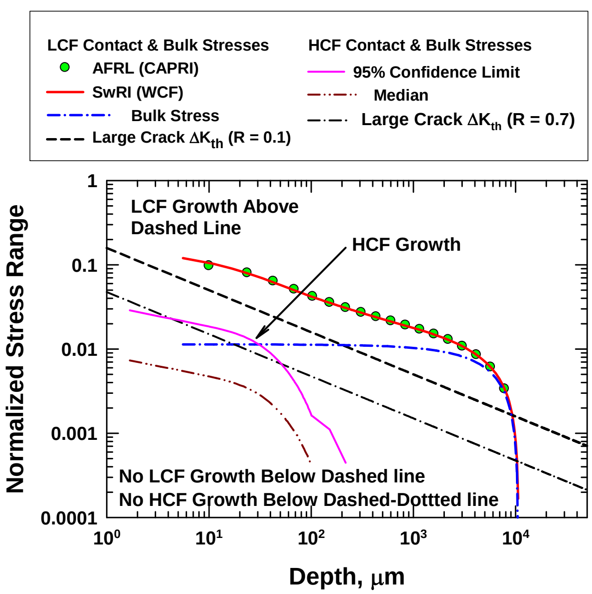

Fig. 14. Comparison of the LCF and HCF stresses against the threshold stresses for fatigue crack growth for stress ratio, R, values of 0.1 and 0.7.

Furthermore, HCF crack growth occurs at a high stress ratio, R, of 0.7. Figure 14 demonstrates that the 95% confidence limit of the HCF stress are on the order of the bulk stresses and exceed the crack growth threshold for R = 0.7 only at crack depth less than about 100 μm. Nonetheless, the crack growth life is reduced and the risk of fracture is increased because of a large number of HCF cycles. Since the number of HCF cycles increases with increasing flutter time duration, the general trend is that the flight hours are reduced with increasing flutter time durations (*i.e.,* increasing number of HCF cycles in the mission profile). Once the crack goes deeper than the HCF contact stress zone, the HCF stresses become very small; the flutter time duration becomes unimportant and FCG is driven solely by the LCF contact and bulk stresses. Figure 14 also suggests that because of a shallow depth (less than 100-200 μm), the HCF contact stresses may be mitigated by surface residual stresses induced by laser-shock peening, low plasticity burnishing or shot peening [3]. Future work will focus on evaluating the effects of a longer flutter time duration, random flutter time durations, and the presence of surface residual stresses on the risk of disk fracture.

7 CONCLUSIONS

A methodology to assess the influence of HCF loading on probabilistic risk in a typical gas turbine engine component has been developed. Based on this study the following conclusions are drawn:

1. LCF and HCF fretting fatigue at the blade/disk interface may be simulated by appending the HCF loads to the end of the LCF loads derived from the mission profile.
2. The number of HCF cycles may be estimated from the flutter frequency and the time duration of flutter using engine data generated to map out the stall flutter regions.
3. HCF contact stresses and crack growth occur at a high R ratio of 0.7 in a region that extends up to about 100 to 200 μm from the contact surface.
4. For the flutter durations and HCF stresses considered, high-cycle fretting fatigue reduced the computed crack growth life by 39 to 65% compared to LCF life without the HCF loads.
5. The presence of HCF loads in the mission profile can significantly increase the risk of disk fracture compared to LCF loads alone.

ACKNOWLEDGEMENTS

This work was supported by NAVAIR under Agreement EDO-08-SA-0021. The computational FEM analyses are performed using the DoD High Performance Computing Modernization Program (HPCMP) support. The assistance by Dr. Wuwei Liang, Mr. Jonathan Moody, and Ms. Loretta Mesa, all of SwRI, are acknowledged.

REFERENCES

[1] Chandra R, Golden PJ, Enright MP, Chan KS, 2008. "Fretting fatigue-based risk assessment of gas turbine engine disks." *49th AIAA Structures, Structural Dynamics, and Materials Conference,* Paper AIAA-2008-2227, April 7-10, 2008, Schaumburg, Illinois.

[2] Enright MP, Chan KS, Moody JP, Golden PJ, Chandra R, Pentz AC, 2009. "Probabilistic fretting fatigue

assessment of aircraft engine disks." *Proceedings of ASME Turbo Expo 2009, Power for Land, Sea, and Air,* Paper GT2009-60224, June 8-12, 2009, Orlando, Florida. *ASME J. of Engineering for Gas Turbines and Power, Vol. 132, July 2010, pp. 0725002-1:072502-9.*

[3] Chan KS, Enright MP, Moody JP, Golden PJ, Chandra R, Pentz AC, 2010. "Residual stress profiles for mitigating fretting fatigue in gas turbine engine disks." *International Journal of Fatigue*, Vol. 32, 2010, pp. 815-823.

[4] Enright MP, Chan KS, Moody JP, Golden P, Chandra R, Pentz A, 2009. "Influence of random residual stress on fretting fatigue risk of engine disks." *AIAA Journal,* AIAA (In Press). Also published in *Proceedings, 50th AIAA Structures, Structural Dynamics, and Materials Conference,* Palm Springs, California, May 4-9, 2009, Paper AIAA-2009-2302.

[5] Golden PJ, Calcaterra J, 2006. "A fracture mechanics life prediction methodology applied to dovetail fretting." *Tribology International*, Vol. 39, pp. 1172-80.

[6] McVeigh PA, Harish G, Farris TN, Szolwinski, MP, 1999. "Modeling interfacial conditions in nominally flat contacts for application to fretting fatigue of turbine engine components." *International Journal of Fatigue*, Vol. 21, pp. S157–65.

[7] Chan KS, Lee Y-D, Davidson DL, Hudak SJ, 2001. "A fracture mechanics approach to high cycle fretting fatigue base on the worst case fret concept." *International Journal of Fracture*, Vol. 112, pp. 299-330.

[8] Wu YT, Enright MP, Millwater HR, 2002. "Probabilistic methods for design assessment of reliability with inspection." *AIAA Journal*, Vol. 40, No. 5, pp. 937-946.

[9] Nicholas T, 1999. "Critical issues in high cycle fatigue." *International Journal of Fatigue*, Vol. 21, pp. S221-S231.

[10] Cowles BA, 1996. "High cycle fatigue in aircraft gas turbines – an industry perspective." *International Journal of Fracture*, Vol. 80, pp. 147-163.

[11] Seinturier E, 2007. "Forced response computation for bladed disks industrial practices and advanced methods." *Proceedings of 12th IFToMM World Congress, Besançon, France,* June 18-21, 2007, pp. 1-17.

[12] Srinivasan AV, 1997. "Flutter and resonant vibration characteristics of engine blades." *Journal of Engineering for Gas Turbines and Power*, Vol. 119, pp. 743-775.

[13] Bréard C, Vahdati M, Sayma AI, Imregun M, 2002. "An integrated time-domain aeroelasticity model for the prediction of fan forced response due to inlet distortion." *ASME Journal of Engineering for Gas Turbines and Power,* Vol. 124, pp. 197-208.

[14] Manwaring SR, Rabe DC, Lorence CB, Wadia, AR, 1997. "Inlet distortion generated forced response of a low-aspect-ratio transonic fan." ASME *Journal of Turbomachinery*, Vol. 119, pp. 665-676.

[15] Gallagher JP *et al*. 2004. "Advanced High Cycle Fatigue (HCF) life assurance methodologies." AFRL-ML-WP-TR-2005-4102, July 2004.

[16] Hilbert GR *et al*. 1998. "Forced response prediction of gas turbine rotor blades. *3rd National Turbine Engine High Cycle Fatigue Conference,* San Antonio, Texas, 1998.

[17] Marshall JG, Green JS, 1998. "Application of a time-linearized Euler method to forced response in a high-pressure turbine and comparison with engine test results." *3rd National Turbine Engine High Cycle Fatigue Conference,* San Antonio, Texas, 1998.

[18] Sayma AI *et al.*, 2001. "Forced response analysis of a vertical take-off lift fan in aircraft configuration." *6th National Turbine Engine High Cycle Fatigue Conference,* Jacksonville, Florida, 2001.

[19] Panovsky J *et al.*, 2002. "Comparisons of experimental and computational forced response in a high pressure turbine." *7th National Turbine Engine High Cycle Fatigue Conference,* Palm Beach Gardens, Florida, 2002.

[20] Petrov EP, 2004. "Direct parametric analysis of forced nonlinear response of bladed disk with contact interfaces." *9th National Turbine Engine High Cycle Fatigue Conference,* Pinehurst, North Carolina, 2004.

[21] Kenyon JA, Griffin JH, 2002. "Maximum mistuned forced response demonstrated on experimental bladed disk." *7th National Turbine Engine High Cycle Fatigue Conference,* May 14-17, 2002, Palm Beach, Florida.

[22] Sanders AJ, Rabe D, Fost R, 2002. "An experimental investigation of stall flutter in an advanced design low-aspect ratio fan blisk." *7th National Turbine Engine High Cycle Fatigue Conference,* May 14-17, 2002, Palm Beach, Florida.

[23] Calcaterra J, Naboulsi S, 2005. "Design methodology to investigate contact fatigue damage in turbine engine hardware." *International Journal of Fatigue*, Vol. 27, 2005, pp. 1133-41.

[24] Golden PJ, 2009. "Development of a dovetail fretting fatigue fixture for turbine engine materials," *International Journal of Fatigue*, Vol. 31, 2009, pp. 620-628.

[25] ABAQUS Documentation, 2007, Simulia, Providence, Rhode Island.

[26] Gean MC, Farris TN, 2005. "Finite element analysis of the mechanics of blade/disk contacts." *46th AIAA Structures, Structural Dynamics, and Materials Conference*, Austin, Texas, April 18-21, 2005.

[27] El Haddad MH, Smith KN, Topper TH, 1979. "Fatigue crack propagation of short cracks." *ASME J Eng Mat Tech,* Vol. 101, pp. 42-46.

[28] NASGRO® Fracture Mechanics and Fatigue Crack Growth Analysis Software, v5.0, NASA-JSC and Southwest Research Institute, San Antonio, Texas, 2006.

[29] Newman Jr JC, 1984. "A crack-opening stress equation for fatigue crack growth." *Int. J. Fracture*, Vol. 24, pp. R131-R135.

[30] "DARWIN® User's Guide," 2008. Southwest Research Institute, San Antonio, Texas.